https://doi.org/10.1016/j.clay.2021.106155

Nanoscale Friction Characteristics of Hydrated Montmorillonites Using Molecular Dynamics

Peng-Chang Wei [‡,a,b], Li-Lan Zhang [‡,a,b], Yuan-Yuan Zheng [*, a,b], Qiu-Feng Diao [a,b], Dao-Yang Zhuang [a,b], Zhen-Yu Yin [c]

[a] School of Civil Engineering, Sun Yat-Sen University, Guangzhou 510275, China

[b] Southern Marine Science and Engineering Guangdong Laboratory (Zhuhai), Zhuhai 519082, China

[c] Department of Civil and Environmental Engineering, The Hong Kong Polytechnic University, Hung Hom, Kowloon, Hong Kong, China

‡ These authors contributed equally to this work

* Corresponding author: Dr. Yuan-Yuan ZHENG, Tel: +86 180 2245 0508;

E-mail: zhengyy57@mail.sysu.edu.cn; zyy378@hotmail.fr

Address: School of Civil Engineering, Zhuhai Campus of Sun Yat-Sen University, Tang Jia Wan, Zhuhai City, 519082, P. R. China

Abstract: The interparticle friction behavior of saturated clay controls its mechanical properties, but remains unclear at nanoscale. As one of major clay minerals, the hydrated montmorillonite (MMT) is selected to investigate the nanoscale friction characteristics using Molecular Dynamics simulation method. Two portions of MMT representing two particles with a water film in the middle are created to simulate an undrained system. A virtual spring is applied on the upper MMT portion to provide the sliding with a constant velocity relative to the bottom portion. The effects of normal load and sliding velocity on the frictional behavior are then investigated. The friction coefficients of hydrated MMT at different cases were measured and compared with other experimental and simulation results for the validation. The evolution of normal load with the number of hydrogen bonds for hydrated MMT was finally analyzed. All simulation results indicated that the friction load fluctuated periodically with a cycle of about 9.10 Å at sliding velocity inferior 0.001 $Å \cdot fs^{-1}$, which was nearly equal to montmorillonite's lattice constant along the sliding direction; the fluctuation amplitude of the friction load increased with the decreasing sliding velocity; the relationship between the average friction load and the logarithm of sliding velocity followed a power function; the friction coefficient and the cohesion were found to increase approximately linearly with sliding velocity.

Keywords: Hydrated montmorillonite; Molecular Dynamics; Nanoscale friction; Normal load; Sliding velocity

1. Introduction

Soft clay is one of the problematic soils in geotechnical engineering due to its high compressibility, low undrained shear strength, significant time-dependent behavior, etc. (Zou et al., 2018; Salimi and Ghorbani, 2020; Zhu et al., 2020). It is widely distributed in considerable parts of the earth, including many low-land and coastal regions (Hamidi and Marandi, 2018). The complex physical and mechanical properties of soft clay are closely related to its microstructure (Wu, 2018). The clay's deformation is always because of the sliding between particles, and the friction properties between particles are fundamental in determining the mechanical properties of clay. Soft clay contains lots of clay minerals, and the montmorillonite (MMT) is one of major clay minerals (Ajmera and Tiwari, 2012; Zhang et al., 2018), which plays an important role in the mechanical properties of soft clay interacting with water due to its strong water sorption capacity (Zheng and Zaoui, 2011). Previous studies have indicated that MMT had an essential impact on controlling failure strength owing to its weak friction coefficient (Summers and Byerlee, 1977; Shimamoto and Logan, 1981; Tetsuka et al., 2018), low permeability, and high expansibility (Zheng and Zaoui, 2018). The abnormally large slip (50 ~ 80 m) in the 2011 Tohoku-Japan earthquake was attributed to the presence of MMT in the fault zone (Fulton et al., 2013; Ujiie et al., 2013). The micromechanics of clay minerals can essentially determine engineering properties in the soft clay (Zhang et al., 2018; Yang et al., 2019).

Experiments, such as rotary-shear friction test (Kubo and Katayama, 2015; Hirono et al., 2019), biaxial friction test (Tetsuka et al., 2018), and triaxial shear test (Behnsen and Faulkner, 2013) have been employed to study the friction behavior of MMT. Previous studies showed that the friction coefficients of MMT found by experiments were scattered under different test conditions, such as hydration state (Morrow et al., 2017; Tetsuka et al., 2018), temperature (Kubo and

Katayama, 2015), normal stress (Saffer et al., 2001; Hirono et al., 2019), interlayer cation (Behnsen and Faulkner, 2013), and sliding velocity (v) (Saffer et al., 2001). It was found that humidity could reduce the friction strength of MMT (Tetsuka et al., 2018); the dependence of shear stress on normal stress was highly linear (Hirono et al., 2019); the friction stress of MMT related to the sliding velocity and normal stress (Saffer et al., 2001). These studies have significantly advanced the knowledge of the friction behavior on MMT-based soils. However, macroscopic experiments were not able to reveal what happened precisely in the contact surface of particles. There are more basic mechanisms of friction that exist at the atomic scale (Krim, 1996). Thus, it is necessary to extend the research of the friction mechanism of the clay-water system from macro- to micro-scale.

With the rapid development of nanoscience and technology at the end of the 20th century, many mechanical phenomena and their mechanism have been explored from macroscale to nanoscale. Nano-tribology (Hölscher et al., 2008) has been gradually evolving into scientific and technological development in the field of tribology. It has been pointed out that microscopic or atomic scale tribology was a new field that needed to be developed urgently in the future (Winer, 1990). So far, theoretical, experimental, and simulation methods have been well developed in the field of nano-tribology. Atomic force microscopy (AFM) experiment has been performed to study the nanoscale friction behavior of graphene (Ye et al., 2016), polystyrenes (Bistac et al., 2008), diamondlike carbon (Dunckle et al., 2010), and muscovite mica (Erlandsson et al., 1988). Friction Force Microscopy (FFM) (Bhushan and Kulkarni, 1996), Optical Microscope (OM), and Scanning Electron Microscopy (SEM) have been applied to explore the friction effect of nanocomposites (Sirong et al., 2007). Theoretical analysis has also been performed to study thermal activation in

atomic friction (Dong et al., 2012) and the velocity dependence of atomic friction (Gnecco et al., 2000).

Molecular dynamics (MD) simulation is a well-established tool to investigate the sliding friction on graphene in water (Vilhena et al., 2016), the mechanism of friction in rotating carbon nanotube bearings (Cook et al., 2013), and the adhesion of silver nanoparticles on the clay substrates (Tokarský et al., 2010). At most friction processes, sliding can cause heating, deformation, chemical changes, and wear of the system's surface layer, affecting the friction behavior (Wen, 2008). Therefore, the sliding state in nanoscale tribology could directly be affected by the sliding velocity, normal load (F_n), and so on (Zhang and Zhang, 2014). Moreover, many studies in nanoscale tribology also showed that the relationship between friction load and many factors was very complex. For example, the relationship of normal load and friction load may be linear (Mate et al., 1987; Erlandsson et al., 1988; Filleter et al., 2009) or nonlinear (Fusco and Fasolino, 2004; Riedo et al., 2004; Gao et al., 2007; Mo et al., 2009); the relationship of velocity and friction load was found to be logarithmic (Riedo et al., 2003), power exponential (Dong et al., 2012), or linear at low velocity (Müser, 2011); others found that the relation of the logarithmic velocity and friction load followed power exponential (Sang et al., 2001), or linear only at high velocity (Müser, 2011). In nanoscale tribology, many studies have been performed on the nanoscale friction behavior of graphene (Ye et al., 2016), carbon (Dunckle et al., 2010), muscovite mica (Erlandsson et al., 1988), nanocomposites (Sirong et al., 2007), etc. However, the effect of external factors, such as normal load, sliding velocity, etc., on the nanoscale friction behavior of clay minerals remains unknown.

In this study, MD simulations have been performed to investigate the effect of normal load and sliding velocity on the nanoscale friction characteristic of hydrated MMT. The relationship between the friction load (f) and the normal load, as well as the sliding velocity, has been

investigated. The effect of normal load on the number of HBonds for hydrated MMT is analyzed. The evolution of friction load with time and sliding distance, the effect of the sliding velocity on the local deformations of the studied system, the friction coefficient, and the cohesion have also been discussed at the end.

2. Simulation details

2.1. System setup

MMT model introduced by Viani and coworkers (Viani et al., 2002) was used in this work, consisting of an alumina octahedral sheet sandwiched between two silica tetrahedral sheets, with the chemical formula of $Na_{0.75}(Si_{7.75}Al_{0.25})(Al_{3.5}Mg_{0.5})O_{20}(OH)_4 \cdot nH_2O$, shown in Figure 1(a). The lattice parameters of MMT were a = 5.18 Å, b = 8.98 Å, c = 9.60 Å, $\alpha = \gamma = \beta = 90°$. The hydrated MMT model contained two MMT portions sandwiched with a water film, which contained 260 water molecules, as shown in Figure 1(b). The model in this work was to simulate an undrained system, so the water content of the system remained constant. This is a limit case with respect to real clay since there always exist exchanges between interlayer water and free water in larger pores. The upper (containing *up1*, *up2,* and *up3*) and the lower (containing *down1*, *down2,* and *down3*) portions of MMT both consisted of 64 unit cells ($8a \times 4b \times 2c$). The simulation box dimensions were 41.44 Å × 35.92 Å × 90.0 Å, including a vacuum of about 40 Å in the *z*-direction, to avoid the interaction between the neighboring upper and lower portions of MMT due to the periodicity of the *z*-direction. The area of the loading surface (equal to the area of the shear surface, [0 0 1] crystal plane) was 41.44 × 35.92 $Å^2$.

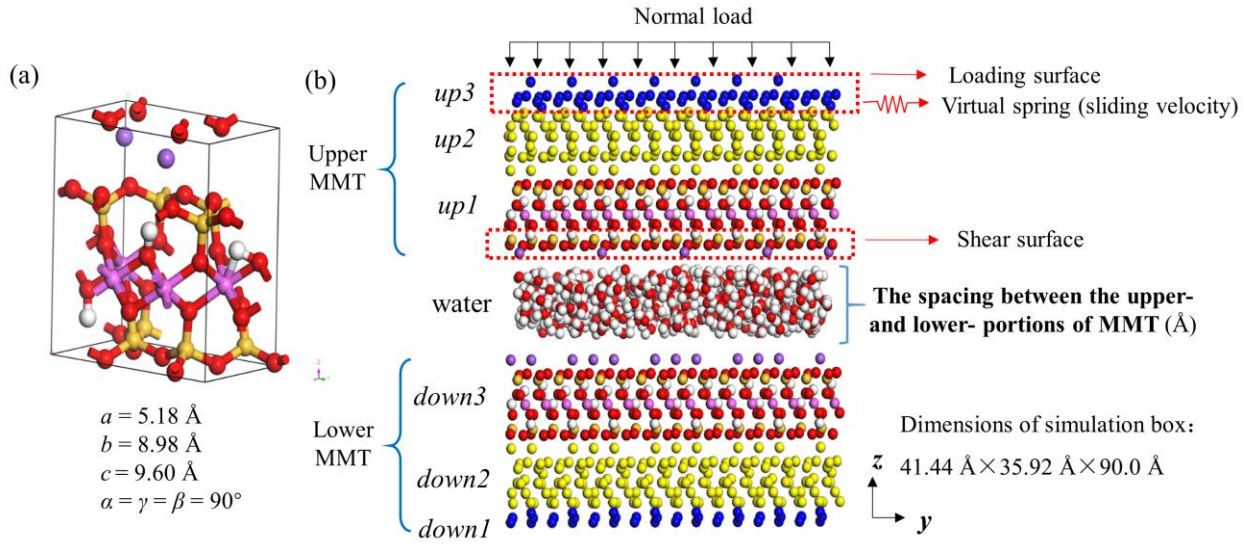

Figure 1. Hydrated MMT model used in this work: (a) Unit cell of MMT ($1a \times 1b \times 1c$); (b) two MMT portions sandwiched with a water film: *down1* (blue) – rigid and fixed the position; *up3* (blue) – rigid and upon applied a normal load and a controlled sliding velocity via a virtual spring along the *y*-direction; *up2* and *down2* (yellow) - temperature-controlled layers; other atoms (colored) - free to move.

The whole simulation model was divided into three parts, the rigid part (blue), the thermal control part (yellow), and the free regions (colored), as shown in Figure 1(b). The *up3* and *down1* sheets were set as rigid bodies (blue), where the *up3* sheet transferred the external vertical loads on the clay-water system without structural deformation, and the *down1* sheet was fixed in its position during the whole simulation. The *up2* and *down2* sheets were set as temperature-controlled layers (yellow) to keep the whole system at a target temperature. The *up1* and *down3* sheets as well as the water film in between, were free to move. The same normal load was applied on each atom of *up3* sheet perpendicular to the clay mineral layers, and a virtual spring was applied on the *up3* sheet to provide a constant sliding velocity along the *y*-direction ([0 1 0] crystal orientation). This virtual spring, at the same time, was used to obtain the friction load between the

two clay mineral portions, which was the sum of the interaction forces between atoms along the *y*-direction. This simulation setting method of the system was drawn from the method presented in the literature (Li and Branicio, 2019).

To test the effect of the stiffness coefficient of the virtual spring on the simulation results, a series of simulations have been carried out with different stiffness of virtual spring, set as 10, 50, 100, 500, and 1000 N/m, under the same conditions with the sliding velocity of virtual spring of 0.001 Å•fs^{-1} and the normal load of 10 GPa. The evolution of the sliding velocity of the upper MMT (v_{MMT}) and the friction load with time under different stiffness coefficients are provided in Figure S1, which can be found online in the Supplementary Material. The stiffness coefficient of the virtual spring had a great influence on the time of the upper MMT portion to achieve the determined velocity. The higher the stiffness coefficient, the faster the velocity of the upper MMT portion approached the virtual spring's velocity. The system with the spring stiffness coefficient of 10 N/m needed at least 100 ps to achieve the equilibrium state, as shown in Figure S1(a), whereas the system with the spring stiffness coefficient superior or equal to 50 N/m required at most 20 ps. On the other hand, the stiffness coefficient of the virtual spring did not affect the result of friction load when the sliding velocity of the upper MMT portion equaled to that of the virtual spring (Figure S1(b)). Therefore, the stiffness coefficient of 100 N/m was selected for all simulations performed in this work to ensure reliability and save computing resources.

2.2. Geometry optimization

MD simulations were performed with LAMMPS (Plimpton, 1995) code. CLAYFF (Cygan et al., 2004) force field was applied in the simulation models, which has been widely used for clay minerals in the MD simulations (Seppälä et al., 2016; Zheng and Zaoui, 2018). The non-bonded and bonded interaction parameters of the CLAYFF force field were taken from the literature

(Cygan et al., 2004). Three-dimensional periodic boundary conditions, the Lennard-Jones potential rule with a cut-off radius of 10 Å, and the Verlet algorithm (Frenkel et al., 1997) for the integral of motion equation were applied in the simulations. The Ewald method (Darden et al., 1993) with an accuracy of 1.0e-6 kcal/mol and a cut-off radius of 8.5 Å were employed for Long-range electrostatic interactions. The water molecule model applied in this work was the SPC water model (Teleman et al., 1987), which has a rigid geometry with an angle of 109.47° and a bond length of 1.0 Å controlled by the SHAKE method. Total potential energy was calculated by equation (1). Energy minimization was applied for geometry optimization using both the steepest descent (SD) method and the conjugate gradient (CG) method. The convergence tolerance was controlled for the energy of 1.0e-12, the force of 1.0e-14 kcal•(mol•Å)$^{-1}$, and the maximum iteration number of 1000.

$$E_{\text{total}} = E_{\text{bond stretch}} + E_{\text{angle bend}} + E_{\text{Coulomb}} + E_{\text{VDW}} \quad (1)$$

where $E_{\text{bond stretch}}$, $E_{\text{angle bend}}$, E_{Coulomb}, and E_{VDW} are bond stretch energy, angle bend energy, coulombic energy, and van der Waals energy, respectively. Only the bond of oxygen and hydrogen (in water or hydroxyl) was included in the bond stretch energy.

$$E_{\text{bond stretch}} = k_1 \left(r_{ij} - r_0 \right)^2 \quad (2)$$

$$E_{\text{angle stretch}} = k_2 \left(\theta_{ijk} - \theta_0 \right)^2 \quad (3)$$

where k_1 is force constant and r_0 represents the equilibrium bond length, both taken from the flexible version of the SPC water model. r_{ij} is the distance between atoms i and j. Only the hydrogen-oxygen-hydrogen angle in water molecule was considered in the angle bend energy, where k_2 is force constant, θ_{ijk} is the bond angle of hydrogen-oxygen-hydrogen, and θ_0 represents the equilibrium bond angle.

$$E_{\mathrm{VDW}} = 4\varepsilon_{ij}\left[\left(\frac{\sigma_{ij}}{r_{ij}}\right)^{12} - \left(\frac{\sigma_{ij}}{r_{ij}}\right)^{6}\right] \quad (4)$$

$$E_{\mathrm{Coulomb}} = \frac{e^2 q_i q_j}{4\pi\varepsilon_0 r_{ij}} \quad (5)$$

where q_i and q_j are the charges of atoms i and j, respectively. ε_0 is the dielectric constant. σ and ε are the size and energy parameters, respectively. Moreover, σ_{ij} and ε_{ij} can be obtained by Mixing Lorentz-Berthelot's law (Frenkel and Smit, 2001), as shown in equations (6) and (7).

$$\sigma_{ij} = \frac{\sigma_i + \sigma_j}{2} \quad (6)$$

$$\varepsilon_{ij} = \sqrt{\varepsilon_i \varepsilon_j} \quad (7)$$

2.3. Relaxation and simulation details

The system was equilibrated for 100 ps with a time step of 1.0 fs with the canonical (NVT) ensemble, using the Langevin algorithm with a damp parameter of 100 to control the temperature of the system; followed by 100 ps with the isothermal-isobaric (NPT) ensemble to ensure the temperature and the pressure of the whole system as defined. The temperature of 300 K and the pressure of 1.0 atm were set during the whole simulation. Subsequently, the system was equilibrated for 100 ps with NVT ensemble at different normal loads. Thereafter, the friction tests were performed for 50 ps with the NVT ensemble through steered molecular dynamics (SMD) at different sliding velocities. However, to better study the friction behavior of the clay-water system in cases at low sliding velocities (0.0001, 0.0005, and 0.001 Å•fs^{-1}), simulation time was extended to ensure the sliding distance of about 100 Å.

3. Results and discussions

3.1. Effect of normal load on friction properties

The relationship between the friction load and the normal loads at the nanoscale is more complex, because the atomic friction process involves complex surface effects such as adhesion effect and surface contact mode etc. (Luan and Robbins, 2005).

To avoid the structural failure of hydrated MMT during friction test due to the normal load exceeding its ultimate strength, a uniaxial compression test was carried out on a dry MMT ($8a \times 4b \times 4c$, containing 128 unit cells) along z-direction ([0 0 1] crystal orientation) at the strain rate of 5×10^{-6} fs^{-1}. The evolution of the stress with the strain of dry MMT along the z-direction is shown in the upper-right corner of Figure 2. The compressive strength of dry MMT obtained from the stress-strain curve was 31.24 GPa, corresponding to a strain of 0.186. Thereafter, the normal load on the hydrated MMT was controlled inferior to 25 GPa in the friction tests.

The evolution of the spacing between the upper and lower portions of MMT with increasing normal loads is shown in Figure 2. This spacing gradually declined from 7.88 to 4.605 Å as the normal load increased, indicating an increase in the contraction of the clay-water system under pressure. Consequently, the energy of the hydrated MMT rose with normal load with the evolution of the increment of energy shown in Figure S2, where the increment is relative to the energy of hydrated MMT at a normal load of 1 atm.

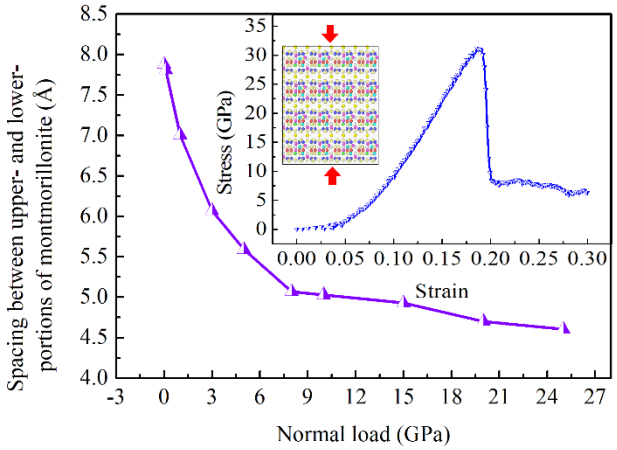

Figure 2. The effect of the normal load on the hydrated MMT: Evolution of the spacing between the upper and lower portions of MMT with normal load during the relaxation with NVT ensemble; the relationship of stress and strain of dry MMT using uniaxial compression test along the *z*-direction at the strain rate of 5×10^{-6} fs^{-1} shown in the upper-right graph.

The narrowing of the space between the upper and lower portions of MMT can also influence the hydrogen bonds (HBonds) network. The effect of normal load on the number of HBonds for hydrated MMT was studied, as shown in Figure 3. For the hydrated MMT system, there are two types of HBonds: (1) the C-W HBonds (Clay-Water) is established between water molecules and the acceptor oxygen atoms of the MMT surface; (2) the W-W HBonds (Water-Water) is established between water molecules. A cut-off distance of 2.4 Å for O…H and an angle cut-off of 30° in H…O-O was employed to set the criterion for the formation of the HBonds, presented by Martí (Martí, 1999). The number of the C-W and the W-W HBonds in the hydrated MMT under different normal loads during the simulation were shown in Figure S3(a) and (b), respectively. The average number of HBonds of the latter 80 ps during the relaxation varied with the normal load, shown in Figure 3(a). The higher the normal load, the faster the formation of the HBonds, the more the number of the HBonds as well as the average number of total HBonds per water molecule (Figure 3(b)).

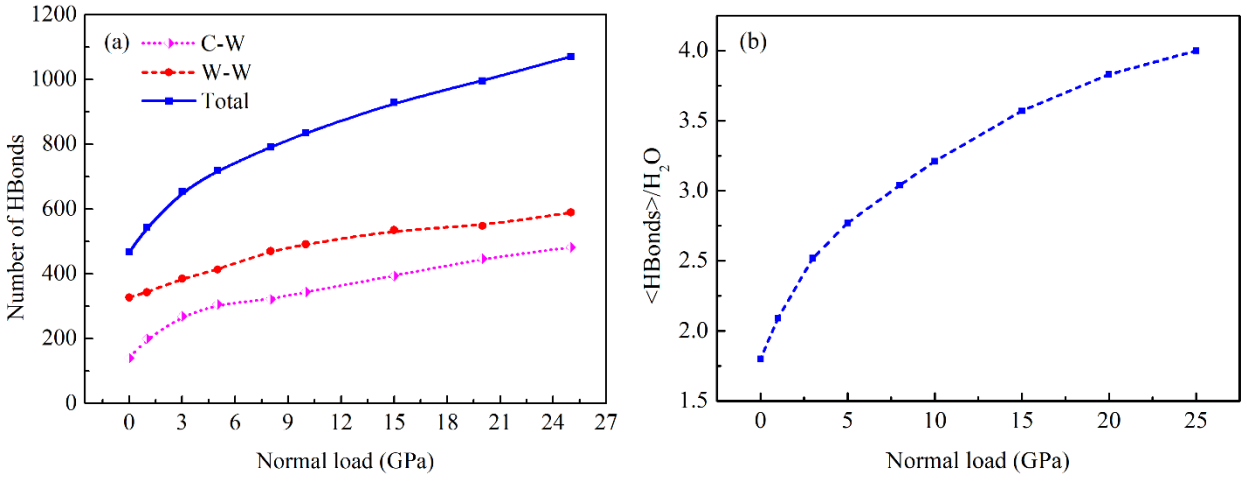

Figure 3. The effect of normal load on the number of the HBonds in hydrated MMT: (a) Evolution of the average number for the latter 80 ps of C-W (Clay - Water), W-W (Water-Water), and total HBonds with the normal load; (b) Average number of total HBonds per water molecule.

The distribution of oxygen and hydrogen in the water film at different normal loads is shown in Figure 4. The peak in the density profile curve of oxygen can be interpreted as an approximate number of layers of water molecules (Abbasi et al., 2020). As shown in Figure 4(a), it was a two-layer water film under the normal load of 1 atm; with the increasing normal load, the water molecules redistributed and formed an unstable three-layer water film at 1 GPa, and then a stable three-layer water film under loads over 5 GPa. As the normal load rose, the intermediate peak of the number density of the oxygen increased. With the increasing normal load, the distribution of oxygens and hydrogens of free water molecules trended to be in a plane (Figure 4(b)), which resulted in the concentration of the distribution of oxygen of free water, and then the augmentation of the W-W HBonds number (Figure S3(b)). On the other hand, the distance between the nearby water molecules and the MMT surface gradually decreased as the normal load increased. Moreover, the hydrogens were close to the MMT surfaces with the increasing normal load, and then entered the MMT surface constantly at normal load over 5 GPa (Figure 4(b)), corresponding to the blue

line crossing the black dotted line (Figure 4(a)). Therefore, under a high normal load, it favored the formation of the C-W HBonds, which indicated the number of the C-W HBonds increasing with the normal load.

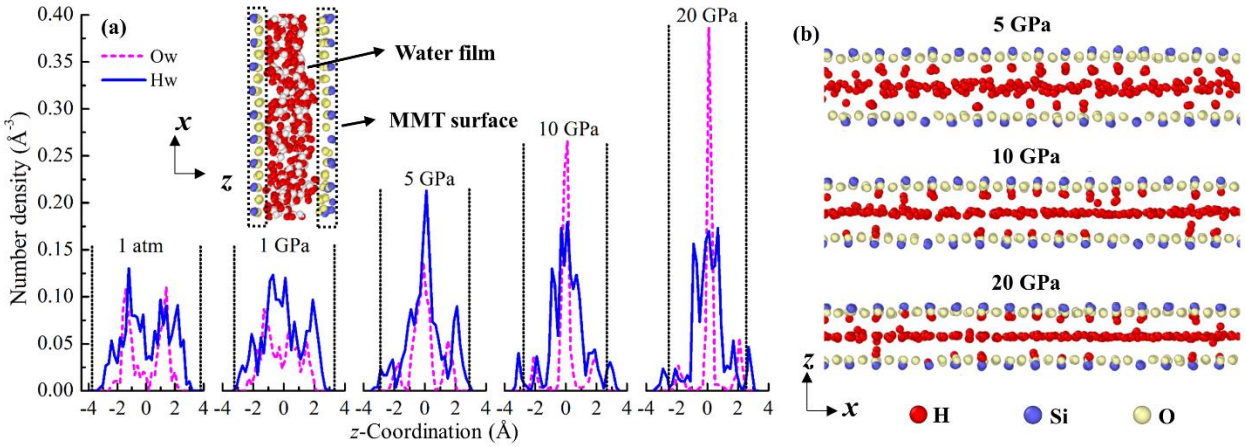

Figure 4. The effect of normal load on the distribution of water molecules between MMT portions: (a) The number density profile of oxygen (Ow) and hydrogen (Hw) in the water film at different normal loads, where the zero corresponds to the center of the interlaminar space, and the black dotted lines represent the MMT surface; a small slice of thickness for each chunk is 0.2 Å. (b) The distribution of interlayer hydrogen between MMT surface sheets, only hydrogen of water molecules as well as silicon and oxygen of MMT surface are rendered for better illustration.

Additionally, the shear stress (average friction load divided by shear surface area) augmented with the normal load, as shown in Figure 5. The shear stress followed a linear relationship with normal loads, which had the same tendency for the cases at different velocities. This similar relationship was also found in some previous researches, such as the friction properties of the muscovite mica using AFM (Erlandsson et al., 1988) and graphene films using means of angle-resolved photoemission spectroscopy (Filleter et al., 2009). The narrowing of the space between the upper and lower portions of MMT with increasing normal load, results in reducing the distance between the MMT surface atoms, which augments the interlayer attraction, the number of total

HBonds and water layers at the interlaminar space, as well as the energy of the system. Therefore, the higher the normal load, the more energy is needed to overcome these interlayer interactions to slide, resulted in a continuous increase of the friction load.

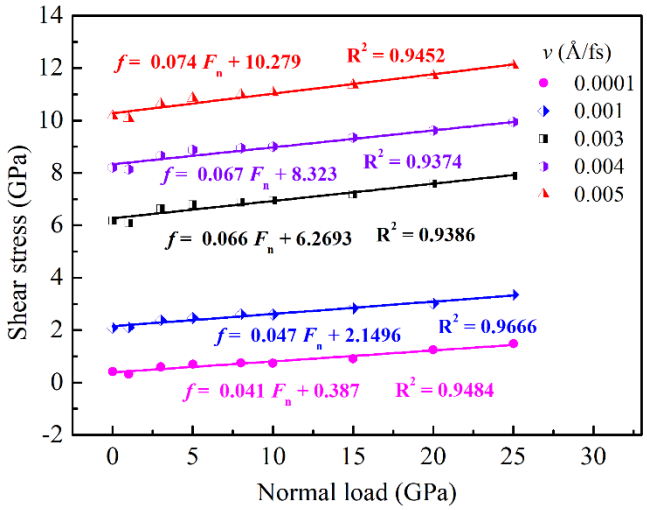

Figure 5. Evolution of shear stress with normal load at different sliding velocities.

3.2. Effect of sliding velocity on friction properties

The evolution of the friction load with time under different sliding velocities in the hydrated MMT was investigated at a normal load of 10 GPa, as shown in Figure 6(a). At the sliding velocity inferior or equal to 0.003 Å•fs^{-1}, the friction load rose gradually with time, and then fluctuated around a certain value, which indicated that the sliding process reached a relatively stable state. However, at a sliding velocity superior or equal to 0.006 Å•fs^{-1}, friction load rose firstly to its maximum value and then decreased to a certain value.

To explore the bulging phenomenon of the friction load, the cases at the sliding velocity of virtual spring of 0.003, 0.006, and 0.01 Å•fs^{-1} were analyzed and shown in Figure 6(b). Since the existence of the virtual spring in the simulation, the sliding velocity of the upper MMT portion (v_{MMT}) was not exactly the sliding velocity of the virtual spring (v). Thereafter, the displacement of the MMT portion and the virtual spring was not exactly the same with a difference of ΔL, where

ΔL is the difference of the sliding distance between the spring and the upper MMT portion. At the sliding velocity over 0.006 Å•fs^{-1}, the bulging phenomenon of the friction load was attributed to the inconsistent increase of the ΔL and v_{MMT} with time. As shown in Figure 6(b), the v_{MMT} and ΔL are not increasing to the v_{MMTeq} and ΔL_{eq} at the same time at OA stage, where the v_{MMTeq} and ΔL_{eq} are corresponding to the average of v_{MMT} and ΔL during the equilibrium state (DE stage). The asynchronism displacement of the MMT portion and the virtual spring, led to the excess elastic potential energy of the virtual spring accumulating at AB stage and then releasing at BC and CD stages, equilibrating at DE stage in the end. However, the bulging phenomenon was not present at the velocity of 0.003 Å•fs^{-1} due to the increasing consistency of the ΔL and v_{MMT}.

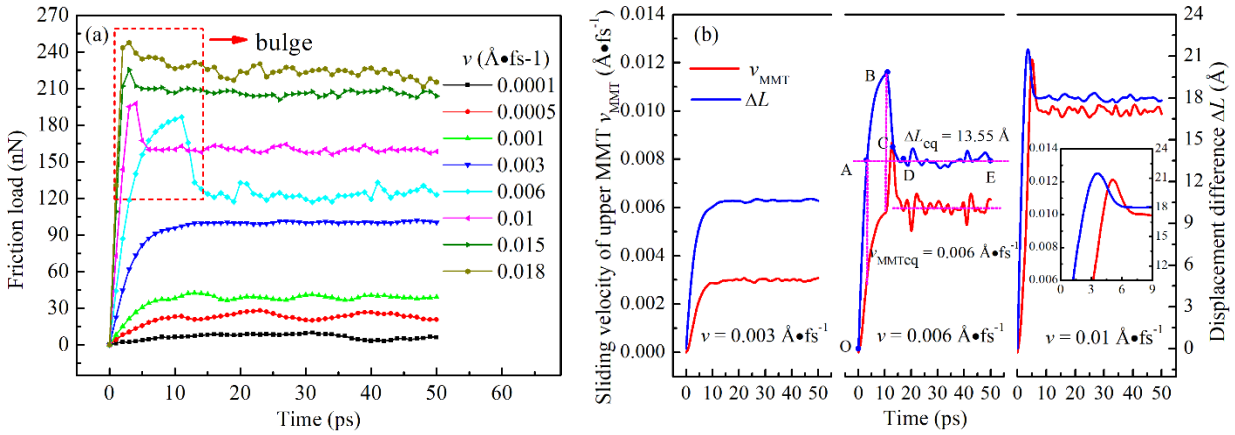

Figure 6. The development of the friction behavior with time for hydrated MMT: (a) evolution of the friction load with time at different sliding velocities at a normal load of 10 GPa; (b) evolution of the sliding velocity of upper MMT (v_{MMT}) and the displacement difference (ΔL) of virtual spring,with time at different sliding velocity (v), where ΔL is the difference of the sliding distance between the spring and the upper MMT portion.; ΔL_{eq} is the average of ΔL during the equilibrium state (DE stage); v_{MMTeq}: the average of v_{MMT} during the equilibrium state (DE stage).

The evolution of friction load with sliding distance at different sliding velocities was shown in Figure 7. The friction load presented a periodic crenelated wave phenomenon at the sliding

velocity inferior or equal to 0.001 Å•fs^{-1}, illustrating that the stick-slip effect (Mate et al., 1987) existed in the sliding process. The fluctuation of friction load presented a periodicity with sliding distance, and the cycle was approximately equal to montmorillonite's lattice constant of 8.98 Å (Figure S4(a) and (b)) along the sliding direction (*y*-direction). As the MMT portion slides, the distance between the adjacent surface atoms changes, then the interaction between these atoms alters accordingly. The slower the sliding velocity, the easier this interaction to be generated; thereafter, the more energy is required to break these interactions and slide. As a result, the fluctuation amplitude of the friction load increases with decreasing sliding velocity. However, the fluctuation is negligible at a sliding velocity greater than 0.001 Å•fs^{-1}.

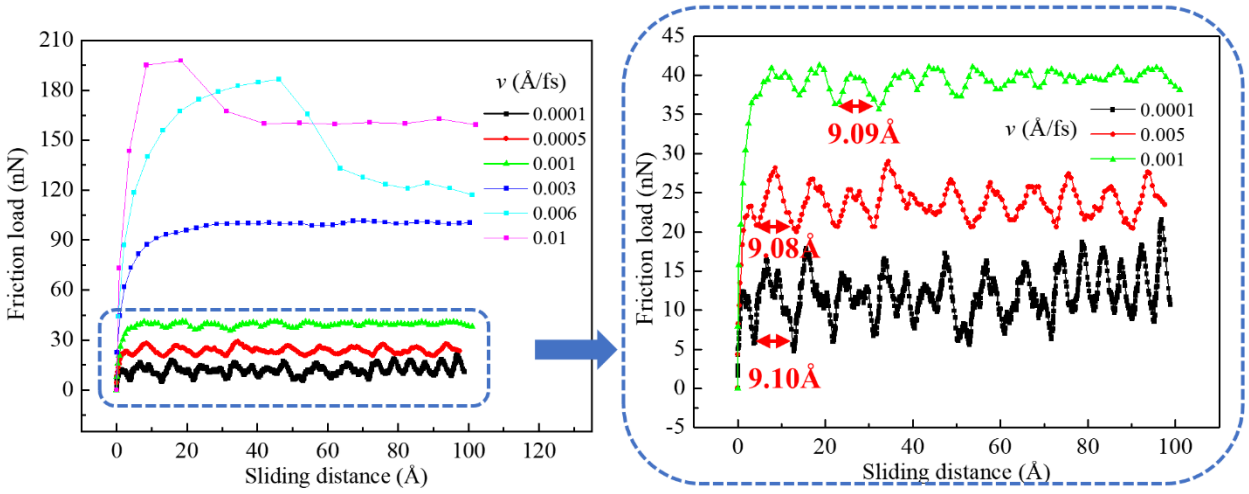

Figure 7. The effect of sliding velocity (*v*) on the friction behavior of hydrated MMT: Evolution of friction load with sliding distance at a normal load of 10 GPa.

The friction coefficient (μ) can be obtained via equation (8),

$$f = \mu F_n + F_0 \tag{8}$$

where f is the friction load, μ the friction coefficient, F_n the applied normal force, and F_0 the offset friction load when $F_n = 0$.

Fitting from the curves of shear and normal stress (Figure 5), the friction coefficient (μ) found in this work were 0.041, 0.047, 0.066, 0.067, and 0.074, corresponding to sliding velocities of 0.0001, 0.001, 0.003, 0.004, and 0.005 Å•fs^{-1}, respectively. Although the friction coefficient of hydrated MMT increased with the sliding velocity, it was still ultra-low on the MMT surface (Summers and Byerlee, 1977; Shimamoto and Logan, 1981; Tetsuka et al., 2018). Results in this work as well as those of the available experiments and simulations, were collected and shown in Table 1. The friction coefficients found in this work agreed well with the previous researches (Liu et al., 1998; Ikari et al., 2007; Takahashi et al., 2007; Behnsen and Faulkner, 2013; Morrow et al., 2017; Tetsuka et al., 2018; Hirono et al., 2019; Abbasi et al., 2020). The existence of minor differences between results in this work and previous results, maybe due to the difference in the scale effect (macro- and micro-scale), hydrated degree, sliding velocity, etc.

Table 1. Friction coefficient (μ) of hydrated MMT at room temperature (300 K) compared to previous experimental and simulation results.

Friction coefficient (μ)	Notes
0.041, 0.047, 0.066, 0.067, and 0.074	Simulation results of this work, corresponding to the sliding velocity of 0.0001, 0.001, 0.003, 0.004, and 0.005 Å • fs^{-1}, respectively, at room temperature.
0.058 (Abbasi et al., 2020)	The average friction coefficient of Na-MMT with the water content of 10% ~ 40% obtained by a shear test using MD simulation, at a temperature of 300K, normal stress of 5 ~ 12.5 GPa, and a constant shear strain rate of 2×10^9 s^{-1}.
0 ~ 0.130 (Liu et al., 1998)	Using the AFM test, the value of the friction coefficient of mica depends on the lateral scan size and a scan rate of AFM.
0.018, 0.055, 0.064 (Hirono et al., 2019)	Rotary-shear friction test, at different shear stresses (initial shear strength, peak shear stress and dynamic shear stress, respectively).
0.030 ~ 0.220 (Tetsuka et al., 2018)	Biaxial friction testing (Ca-MMT), at different humidifies (11% ± 1 ~ 93 ± 7%) and normal stress of 10 MPa.

0.060 ~ 0.330 (Tetsuka et al., 2018)	Biaxial friction testing (Na-MMT), at different humidifies (10% ± 1 ~ 91 ± 7%) and normal stress of 10 MPa.
0.100 ~ 0.280 (Morrow et al., 2017)	Shear test, at room temperature and the range of normal stress 0 ~700MPa.
0.110 (Ca-MMT and Mg-MMT), 0.150 (Na-MMT), 0.260 (K-MMT) (Behnsen and Faulkner, 2013)	Triaxial shear test, at the range of normal stress 10 ~ 100 MPa and loading rate of 0.5 μm/s.
0.150 ~ 0.320 (Saffer et al., 2001)	Shear test, at room temperature, room humidity, and range of normal stress 5 ~ 45 MPa.
0.120 (Behnsen and Faulkner, 2012)	Triaxial deformation apparatus, at a range of normal stress 5 MPa ~ 100 MPa.
0.120 (Tembe et al., 2010)	Conventional triaxial compression tests, at room temperature and normal stress of 40 MPa.
0.100 (Takahashi et al., 2007)	A triaxial testing machine, at room temperature.
0.090 ~ 0.480 (Ikari et al., 2007)	Biaxial stress experiments.

Duque-Redondo et al. (Duque-Redondo et al., 2014) proposed that the cohesion (c) between clay sheets may have two origins: the electrostatic interactions between the charged clay mineral sheets and the interlaminar cations; and the hydrogen-bond network among water molecules and the clay mineral surface. The cohesion in this work was defined as the shear stress value, obtained as offset friction load (F_0) divided by shear surface area. The cohesion of 0.387 GPa was found at the sliding velocity of 0.0001 Å•fs^{-1}, close to the cohesion range of 0.026 ~ 0.346 GPa for hydrated Na-MMT (Abbasi et al., 2020) through a shear test with a constant shear strain rate of 2×10^9 s^{-1} using MD simulation. Furthermore, as shown in Figure 8(a), both the cohesion and the friction coefficient increased approximately linearly with the sliding velocity, where c^* was 1.0 GPa and v^* was

0.00001 Å•fs^{-1} for the normalization purpose. This finding indicates that the sliding velocity is a critical factor in the friction process of clay minerals.

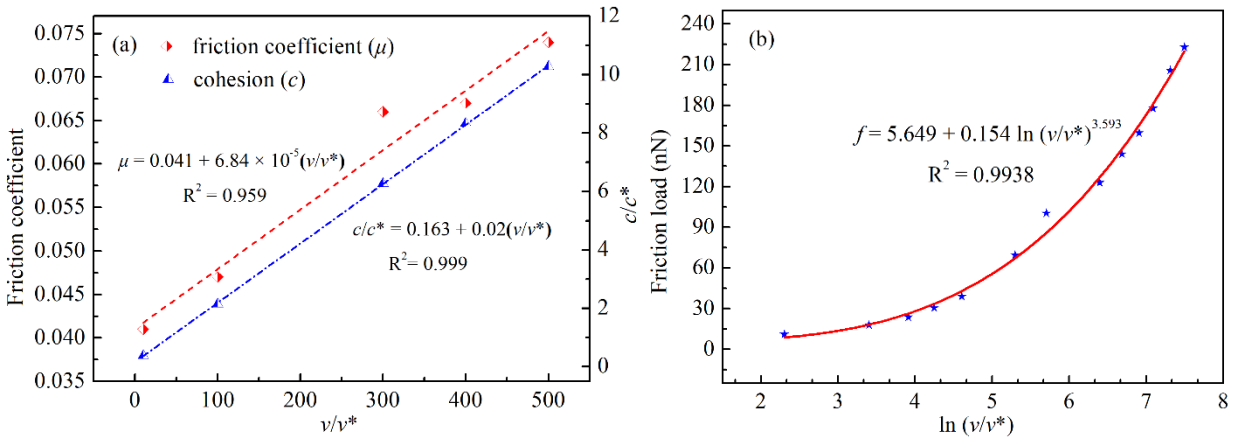

Figure 8. (a) The effect of the sliding velocity (v) on the friction coefficient (μ) and the cohesion (c), where c is shear stress obtained through the offset friction load (F_0) divided by shear surface area, c^* is 1.0 GPa, and v^* is 0.00001 Å•fs^{-1}; (b) evolution of the friction load with ln (v/v^*) at a normal load of 10 GPa.

The average friction load increased with sliding velocity, and their relationship was found as $f \propto \ln(v/v^*)^{3.593}$, shown in Figure 8(b). It is similar to the research of Sang et al. (Sang et al., 2001), which found the power exponential relation ($f \propto (\ln v)^{2/3}$) between the friction load and velocity of the tip in an AFM test, when the tip of AFM was dragged across a surface. The higher the sliding velocity, the more the sliding distance of atomic transition within the same time. In this case, large forces was required to overcome more interlaminar energy. It is significantly distinct from previous studies about classical tribology law (Sang et al., 2001) that friction load was independent of sliding velocity, which may be due to the non-bonded interactions, such as coulombic energy and van der Waals energy, not taken into account in macroscale friction behavior.

To understand the effect of sliding velocity on local deformations of the hydrated MMT system, the local strain tensor proposed by Shimizu et al. (Shimizu et al., 2007) was used to represent the

displacement of a given atom relative to its neighbor. The evolution of the spatial distribution of the local strain for hydrated MMT at a normal load of 10 GPa with sliding velocity was shown in Figure S5**.** At the sliding velocity inferior or equal to 0.003 Å•fs^{-1}, the friction load was dissipated by relaxation of the atoms of the water film and interlaminar surface atoms of the *up1* and the *down3*. When the sliding velocity was greater than 0.006 Å•fs^{-1}, the sliding occurred not only in the water film and the neighboring clay mineral surface, but also inside the upper MMT portion. As the sliding velocity rose, the more deformed atoms for hydrated MMT, the higher the friction load. Therefore, it also provides evidence for the friction load increasing with sliding velocity.

The evolution of temperature with time at different sliding velocities was shown in Figure S6(a). The system's temperature fluctuated around the controlled temperature (300 K) when sliding velocity inferior or equal to 0.001 Å•fs^{-1}. However, the temperature grew remarkably as sliding velocity increased when the sliding velocity greater than 0.003 Å•fs^{-1}. Figure S6(b) shows that the relationship of temperature and sliding velocity is approximately linear, mainly because the high sliding velocity could increase the possibility of atom collisions (Figure S5), and then increase the number of deformed atoms and atomic thermal energy for hydrated MMT.

Furthermore, to explore the effect of the damp parameter of thermostat on the temperature of the system upon friction, three damp parameters (10, 100, and 1000) were studied under the different sliding velocities at the same controlled temperature (300 K). As shown in Figure S7, the temperature of the system increased with the damp parameter at the same sliding velocity. Moreover, the greater the sliding velocity, the greater the influence of damp parameters on the temperature of the system. At the sliding velocity equal to 0.006 Å•fs^{-1}, the temperature of the system with a damp parameter of 10 fluctuated much more wildly than the other two cases. It indicated that the temperature could be well controlled at low sliding velocity but fluctuated wildly

at high velocity (greater than 0.006 Å•fs^{-1}) when the damp parameter of the thermostat was 10. This is consistent with the explanation for the damp parameter of thermostat in LAMMPS (Plimpton, 1995) that the temperature can fluctuate wildly when damp is too small; the temperature will take a very long time to equilibrate when damp is too large, and a good choice for many models is a damp of around 100 timesteps. It is worth noting that the high sliding velocity (greater than 0.006 Å•fs^{-1}) involves a dramatic increase in the temperature of the system and an expansion of the shear strain range of the clay mineral layer in nanoscale tribology. Thus, further works need to be carried out to study the effect of high sliding velocity and temperature on friction properties in nanoscale, which is currently undergoing and will be reported in the future.

4. Conclusions

Molecular Dynamics simulations have been performed to investigate the nanoscale friction behavior of undrained hydrated Montmorillonite (MMT), expanding further studies of nanoscale tribology for clay minerals. The conclusions are made as follows:

(1) The average friction load and the normal load followed an approximately linear relationship. The number of the total HBonds and water layers at the interlaminar space, as well as the energy of the system, could increase with normal load. More energy was needed to overcome the interlayer interactions for sliding, causing a continuous increase of friction load. The frictional coefficient in hydrated MMT was found as 0.041 ~ 0.074, corresponding to 0.0001 ~ 0.005 Å•fs^{-1} of sliding velocities, which agreed well with experimental and simulation results. Moreover, the virtual spring's stiffness coefficient did not affect the simulation results, but the acceleration time to achieve the required velocity of the clay portion.

(2) The average friction load and the logarithm of sliding velocity followed a power function relationship of $f \propto \ln(v/v^*)^{3.593}$ in the sliding process, which indicated that nanoscale tribology is

very different from the classical tribology law of the macroscale. The number of deformed atoms in hydrated MMT increased when the sliding velocity rose. Moreover, both the friction coefficient and the cohesion increased approximately linearly with the sliding velocity.

(3) At sliding velocity inferior or equal to 0.001 Å•fs^{-1}, friction load fluctuated periodically around a certain value, with the cycle approximately equal to montmorillonite's lattice constant along the sliding direction. Furthermore, the fluctuation amplitude increased with decreasing sliding velocity. This work may give an insight into the friction behavior of hydrated clay minerals such as in soft clay.

Author Contributions

‡ **Peng-Chang Wei and Li-Lan Zhang:** Conceptualization, Methodology, Investigation, Data Curation, Writing - Review & Editing, Writing - Original Draft, Visualization; (‡ These authors contributed equally to this work)

Yuan-Yuan Zheng: Conceptualization, Writing-Review & Editing, Supervision; Project administration; Funding acquisition;

Qiu-Feng Diao: Methodology; Software;

Dao-Yang Zhuang: Software;

Zhen-Yu Yin: Writing - Review & Editing, Funding acquisition.

Declaration of Competing Interest

The authors declare no competing financial interest.

Acknowledgments:

This research was financially supported by the National Natural Science Foundation of China (Grant No. 52009149), the Natural Science Foundation of GuangDong Basic and Applied Basic Research Foundation (Grant No. 2021A1515012612), and the Research Grants Council (RGC) of Hong Kong Special Administrative Region Government (HKSARG) of China (Grant No.: 15217220).

References:

Abbasi, B., Muhunthan, B., Salehinia, I. and Zbib, H. M., 2020. Nanoscale Stick-Slip Behavior of Na-Montmorillonite Clay. J. Eng. Mech., 146, 04020138. http://doi.org/10.1061/(ASCE)EM.1943-7889.0001881.

Ajmera, B. and Tiwari, B., 2012. Consolidation Characteristics of Soft Clays with Saline Water As a Pore Fluid, GeoCongress 2012, San Francisco, pp. 1223-1232. http://doi.org/10.1061/9780784412121.126.

Behnsen, J. and Faulkner, D. R., 2012. The effect of mineralogy and effective normal stress on frictional strength of sheet silicates. J. Struct. Geol., 42, 49-61. http://doi.org/10.1016/j.jsg.2012.06.015.

Behnsen, J. and Faulkner, D. R., 2013. Permeability and frictional strength of cation-exchanged montmorillonite. J. Geophys. Res. Solid Earth, 118, 2788-2798. http://doi.org/10.1002/jgrb.50226.

Bhushan, B. and Kulkarni, A. V., 1996. Effect of normal load on microscale friction measurements. Thin Solid Films, 278, 49-56. https://doi.org/10.1016/0040-6090(95)08138-0.

Bistac, S., Schmitt, M., Ghorbal, A., Gnecco, E. and Meyer, E., 2008. Nano-scale friction of polystyrene in air and in vacuum. Polymer, 49, 3780-3784.

http://doi.org/10.1016/j.polymer.2008.06.032.

Cook, E. H., Buehler, M. J. and Spakovszky, Z. S., 2013. Mechanism of friction in rotating carbon nanotube bearings. J. Mech. Phys. Solids, 61, 652-673. http://doi.org/10.1016/j.jmps.2012.08.004.

Cygan, R. T., Liang, J. and Kalinichev, A. G., 2004. Molecular Models of Hydroxide, Oxyhydroxide, and Clay Phases and the Development of a General Force Field. J. Phys. Chem. B, 108, 1255-1266. http://doi.org/10.1021/jp0363287.

Darden, T., York, D. and Pedersen, L., 1993. Particle mesh Ewald: An N · log(N) method for Ewald sums in large systems. J. Chem. Phys., 98, 10089-10092. http://doi.org/10.1063/1.464397.

Dong, Y., Perez, D., Gao, H. and Martini, A., 2012. Thermal activation in atomic friction: revisiting the theoretical analysis. J. Phys.: Condens. Matter, 24, 265001. http://doi.org/10.1088/0953-8984/24/26/265001.

Dowson, D., 1998. History of Tribology. Longman, London.

Dunckle, C. G. et al., 2010. Temperature dependence of single-asperity friction for a diamond on diamondlike carbon interface. J. Appl. Phys., 107, 114903. http://doi.org/10.1063/1.3436564.

Duque-Redondo, E., Manzano, H., Epelde-Elezcano, N., Martinez-Martinez, V. and Lopez-Arbeloa, I., 2014. Molecular Forces Governing Shear and Tensile Failure in Clay-Dye Hybrid Materials. Chem. Mater., 26, 4338-4345. http://doi.org/10.1021/cm500661d.

Erlandsson, R., Hadziioannou, G., Mate, C. M., McClelland, G. M. and Chiang, S., 1988. Atomic scale friction between the muscovite mica cleavage plane and a tungsten tip. J. Chem. Phys., 89, 5190-5193. http://doi.org/10.1063/1.455608.

Filleter, T. et al., 2009. Friction and dissipation in epitaxial graphene films. Phys. Rev. Lett., 102,

086102. http://doi.org/10.1103/PhysRevLett.102.086102.

Frenkel, D. and Smit, B., 2001. Understanding molecular simulation: From algorithms to applications. Academic Press.

Frenkel, D., Smit, B., Tobochnik, J., McKay, S. R. and Christian, W., 1997. Understanding Molecular Simulation. Comput. Phys., 11, 351. http://doi.org/10.1063/1.4822570.

Fulton, P. M. et al., 2013. Low Coseismic Friction on the Tohoku-Oki Fault Determined from Temperature Measurements. Science, 342, 1214-1217. http://doi.org/10.1126/science.1243641.

Fusco, C. and Fasolino, A., 2004. Power-law load dependence of atomic friction. Appl. Phys. Lett., 84, 699-701. http://doi.org/10.1063/1.1644617.

Gao, G., Cannara, R. J., Carpick, R. W. and Harrison, J. A., 2007. Atomic-Scale Friction on Diamond: A Comparison of Different Sliding Directions on (001) and (111) Surfaces Using MD and AFM. Langmuir, 23, 5394-5405. http://doi.org/10.1021/la062254p.

Gnecco, E. et al., 2000. Velocity Dependence of Atomic Friction. Phys. Rev. Lett., 84, 1172-1175. http://doi.org/Velocity Dependence of Atomic Friction.

Hamidi, S. and Marandi, S. M., 2018. Clay concrete and effect of clay minerals types on stabilized soft clay soils by epoxy resin. Appl. Clay Sci., 151, 92-101. http://doi.org/10.1016/j.clay.2017.10.010.

Hirono, T., Tsuda, K. and Kaneki, S., 2019. Role of Weak Materials in Earthquake Rupture Dynamics. Sci Rep, 9. http://doi.org/10.1038/s41598-019-43118-5.

Hölscher, H., Schirmeisen, A. and Schwarz, U. D., 2008. Principles of atomic friction: from sticking atoms to superlubric sliding. Phil. Trans. R. Soc. A., 366, 1383-1404. http://doi.org/10.1098/rsta.2007.2164.

Ikari, M. J., Saffer, D. M. and Marone, C., 2007. Effect of hydration state on the frictional

properties of montmorillonite-based fault gouge. J. Geophys. Res., 112. http://doi.org/10.1029/2006JB004748.

Krim, J., 1996. Friction at the atomic scale. Sci. Am., 275, 74-80. http://doi.org/10.1007/978-94-011-2811-7_21.

Kubo, T. and Katayama, I., 2015. Effect of temperature on the frictional behavior of smectite and illite. J. Miner. Petrol. Sci., 110, 293-299. http://doi.org/10.2465/jmps.150421.

Li, H. and Branicio, P. S., 2019. Ultra-low friction of graphene/C60/graphene coatings for realistic rough surfaces. Carbon, 152, 727-737. http://doi.org/10.1016/j.carbon.2019.06.020.

Liu, E., Blanpain, B., Celis, J. P. and Roos, J. R., 1998. Comparative study between macrotribology and nanotribology. J. Appl. Phys., 84, 4859-4865. http://doi.org/10.1063/1.368728.

Luan, B. and Robbins, M. O., 2005. The breakdown of continuum models for mechanical contacts. Nature, 435, 929-932. http://doi.org/10.1038/nature03700.

Martí, J., 1999. Analysis of the hydrogen bonding and vibrational spectra of supercritical model water by molecular dynamics simulations. J. Chem. Phys., 110, 6876-6886. http://doi.org/10.1063/1.478593.

Mate, C. M., Mcclelland, G. M., Erlandsson, R. and Chiang, S., 1987. Atomic-scale friction of a tungsten tip on a graphite surface. Phys. Rev. Lett., 59, 1942-1945. http://doi.org/10.1103/PhysRevLett.59.1942.

Mo, Y., Turner, K. T. and Szlufarska, I., 2009. Friction laws at the nanoscale. Nature, 457, 1116-1119. http://doi.org/10.1038/nature07748.

Morrow, C. A., Moore, D. E. and Lockner, D. A., 2017. Frictional strength of wet and dry montmorillonite. J. Geophys. Res. Solid Earth, 122, 3392-3409.

http://doi.org/10.1002/2016JB013658.

Müser, M. H., 2011. Velocity dependence of kinetic friction in the Prandtl-Tomlinson model. Phys. Rev. B: Condens. Matter Mater. Phys., 84, 125419. http://doi.org/10.1103/physrevb.84.125419.

Plimpton, S., 1995. Fast Paraller Algorithms for Short-Range Molecular Dynamics. J. Comput. Phys., 117, 1-19. http://doi.org/10.1006/jcph.1995.1039.

Riedo, E., Gnecco, E., Bennewitz, R., Meyer, E. and Brune, H., 2003. Interaction Potential and Hopping Dynamics Governing Sliding Friction. Phys. Rev. Lett., 91, 084502. http://doi.org/10.1103/physrevlett.91.084502.

Riedo, E., Palaci, I., Boragno, C. and Brune, H., 2004. The 2/3 Power Law Dependence of Capillary Force on Normal Load in Nanoscopic Friction. J. Phys. Chem. B, 108, 5324-5328. http://doi.org/10.1021/jp0360624.

Saffer, D. M., Frye, K. M., Marone, C. and Mair, K., 2001. Laboratory results indicating complex and potentially unstable frictional behavior of smectite clay. Geophys. Res. Lett., 28, 2297-2300. http://doi.org/10.1029/2001gl012869.

Salimi, M. and Ghorbani, A., 2020. Mechanical and compressibility characteristics of a soft clay stabilized by slag-based mixtures and geopolymers. Appl. Clay Sci., 184, 105390. http://doi.org/10.1016/j.clay.2019.105390.

Sang, Y., Dube, M. and Grant, M., 2001. Thermal effects on atomic friction. Phys. Rev. Lett., 87, 174301. http://doi.org/10.1103/PhysRevLett.87.174301.

Seppälä, A., Puhakka, E. and Olin, M., 2016. Effect of layer charge on the crystalline swelling of Na+, K+ and Ca2+ montmorillonites: DFT and molecular dynamics studies. Clay Miner., 51, 197-211. http://doi.org/10.1180/claymin.2016.051.2.07.

545 Shimamoto, T. and Logan, J. M., 1981. Effects of simulated clay gouges on the sliding behavior
546 of Tennessee Sandstone. Tectonophysics, 75, 243-255. http://doi.org/10.1016/0040-
547 1951(81)90276-6.
548 Shimizu, F., Ogata, S. and Li, J., 2007. Theory of Shear Banding in Metallic Glasses and
549 Molecular Dynamics Calculations. Mater. Trans., 48, 2923-2927.
550 http://doi.org/10.2320/matertrans.mj20076910.2320/matertrans.mj200769.
551 Sirong, Y., Zhongzhen, Y. and Yiu-Wing, M., 2007. Effects of SEBS-g-MA on tribological
552 behaviour of nylon 66/organoclay nanocomposites. Tribol. Int., 40, 855-862.
553 http://doi.org/10.1016/j.triboint.2006.09.001.
554 Summers, R. and Byerlee, J., 1977. A note on the effect of fault gouge composition on the
555 stability of frictional sliding. Int. J. Rock Mech. Min. Sci. Geome. Abstra., 14, 155-160.
556 https://doi.org/10.1016/0148-9062(77)90007-9.
557 Takahashi, M., Mizoguchi, K., Kitamura, K. and Masuda, K., 2007. Effects of clay content on
558 the frictional strength and fluid transport property of faults. J. Geophys. Res., 112.
559 http://doi.org/10.1029/2006JB004678.
560 Teleman, O., Jonsson, B. and Engstrom, S., 1987. A molecular dynamics simulation of a water
561 model with intramolecular degrees of freedom. Mol. Phys., 60, 193-203.
562 http://doi.org/10.1080/00268978700100141.
563 Tembe, S., Lockner, D. A. and Wong, T., 2010. Effect of clay content and mineralogy on
564 frictional sliding behavior of simulated gouges: Binary and ternary mixtures of quartz, illite,
565 and montmorillonite. J. Geophys. Res., 115, B03416. http://doi.org/10.1029/2009jb006383.
566 Tetsuka, H., Katayama, I., Sakuma, H. and Tamura, K., 2018. Effects of humidity and interlayer
567 cations on the frictional strength of montmorillonite. Earth Planets Space, 70.

http://doi.org/10.1186/s40623-018-0829-1.

Tokarský, J. et al., 2010. Adhesion of silver nanoparticles on the clay substrates; modeling and experiment. Appl. Surf. Sci., 256, 2841-2848. http://doi.org/10.1016/j.apsusc.2009.11.037.

Ujiie, K. et al., 2013. Low Coseismic Shear Stress on the Tohoku-Oki Megathrust Determined from Laboratory Experiments. Science, 342, 1211-1214. http://doi.org/10.1126/science.1243485.

Viani, A., Gualtieri, A. F. and Artioli, G., 2002. The nature of disorder in montmorillonite by simulation of X-ray powder patterns. Am. Mineral., 87, 966-975. http://doi.org/10.2138/am-2002-0720.

Vilhena, J. G. et al., 2016. Atomic-Scale Sliding Friction on Graphene in Water. ACS Nano, 10, 4288-4293. http://doi.org/10.1021/acsnano.5b07825.

Wen, S., 2008. Principles of Tribology. Tsinghua University Press, BeiJing.

Winer, W. O., 1990. Future trends in tribology. Wear, 136, 19-27. http://doi.org/10.1016/0043-1648(90)90069-M.

Wu, J., 2018. Analysis of Mechanical Response and Microstructure of Soft Clay under Different Shear Strain Rates, Guangdong University of Technology, pp 94. http://doi.org/CNKI:CDMD:2.1018.866941.

Yang, H., He, M., Lu, C. and Gong, W., 2019. Deformation and failure processes of kaolinite under tension: Insights from molecular dynamics simulations. Sci. China Phys. Mech. Astron., 62, 064612. http://doi.org/10.1007/s11433-018-9316-3.

Ye, Z. et al., 2016. Load-Dependent Friction Hysteresis on Graphene. ACS Nano, 10, 5161-5168. http://doi.org/10.1021/acsnano.6b00639.

Zhang, H. and Zhang, T., 2014. Recent Progress in Atomic-scale Friction. Chin. J. Solid Mech.,

35, 417-440. http://doi.org/CNKI:SUN:GTLX.0.2014-05-001.

Zhang, J., Pervukhina, M. and Clennell, M. B., 2018. Nanoscale elastic properties of dry and wet smectite. Clays Clay Miner, 66, 209-219. http://doi.org/10.1346/CCMN.2018.064094.

Zhang, T., Deng, Y., Wu, Z., Liu, S. and Liu, Y., 2018. Engineering behavior and constitutive model of artificial soft clay considering pore water salinity effect. Chinese Journal of Geotechnical Engineering, 40, 1690-1697. http://doi.org/10.11779/CJGE201809016.

Zheng, Y. and Zaoui, A., 2011. How water and counterions diffuse into the hydrated montmorillonite. Solid State Ionics, 203, 80-85. http://doi.org/10.1016/j.ssi.2011.09.020.

Zheng, Y. and Zaoui, A., 2018. Mechanical behavior in hydrated Na-montmorillonite clay. Phys. A., 505, 582-590. http://doi.org/10.1016/j.physa.2018.03.093.

Zhu, J., Zhao, H., Luo, Z. and Liu, H., 2020. Investigation of the mechanical behavior of soft clay under combined shield construction and ocean waves. Ocean Eng., 206, 107250. http://doi.org/10.1016/j.oceaneng.2020.107250.

Zou, S., Xie, X., Li, J., Wang, Z. and Wang, H., 2018. Rheological characteristics and one-dimensional isotache modelling of marine soft clays. Mar. Georesour. Geotec., 37, 660-670. http://doi.org/10.1080/1064119x.2018.1473903.